

Nanocalorimetry of Nanoscaled Ni/Al Multilayer Films: On the Methodology to Determine Reaction Kinetics for Highly Reactive Films

Sascha S. Riegler,* Yesenia H. Sauni Camposano, Konrad Jaekel, Maximilian Frey, Christian Neemann, Sebastian Matthes, Emina Vardo, Maryam R. Chegeni, Heike Bartsch, Ralf Busch, Jens Müller, Peter Schaaf, and Isabella Gallino

Free-standing Ni/Al multilayer films with a planar morphology, a bilayer thickness of 20 nm, and an average composition of Ni₅₀Al₅₀ (at%) deposited by direct current magnetron sputtering are investigated by nanocalorimetry and conventional calorimetry. Both the novel fast differential scanning calorimeter (FDSC) Flash DSC 2+ from Mettler–Toledo (MT) and conventional calorimeter MT DSC 3 are used to cover a range of heating rates from 0.1 to 10⁴ K s⁻¹. A quantitative kinetic study of the interdiffusion and phase reaction sequence is performed via a Kissinger analysis covering five orders of magnitude of heating rates. Using the calorimetric data, the derived apparent activation energies suggest monotonic reaction kinetics over the entire range of heating rates applied. To correct the thermal lag at the highest heating rates with the FDSC for nonadhered free-standing films, a new methodology for its correction is used. Overall, this work extends the application of commercial FDSC to nonadhered films.

intermetallic compound.^[1] The highly energetic nature of those systems enables the possibility of self-sustaining high-temperature synthesis (SHS) reactions provided the heat release from the multilayer system is larger than the heat absorbed by the surroundings of the system.^[2] That means the reaction can propagate through the remaining material without any further external energy input. This unique property enables different applications such as a localized heat source for room-temperature soldering of materials with different thermal expansion coefficients^[3,4] or micropropulsion units,^[5] in self-healing of materials^[6] or synthesis of high-temperature materials.^[7] Beyond applications in engineering, these systems find interest in scientific research regarding the influence of interfaces on the reaction sequence

1. Introduction

Metallic multilayer films based on Al-X pairs with micro- and nanoscale morphology have attracted interest from the scientific community due to their high interface density, allowing the investigation of highly nonequilibrium systems compared to bulk systems. Preferred metal pairs include those that show a large negative enthalpy of formation of the aluminide

in nanometric material systems. Nanoscaled multilayers produced by physical vapor deposition (PVD) allow well-defined states to be manufactured for scientific investigations. This approach provides a clearer property–microstructure–correlation than, e.g., samples produced by cold rolling^[8] or high-pressure torsion (HPT).^[9]


Most previous calorimetric studies on nanoscaled multilayers were performed with heating rates slower than 2 K s⁻¹ due to the

S. S. Riegler, M. Frey, C. Neemann, M. R. Chegeni, R. Busch, I. Gallino
Institute for Metallic Materials
Saarland University
Campus C6.3, 66123 Saarbrücken, Germany
E-mail: sascha.riegler@uni-saarland.de

Y. H. Sauni Camposano, S. Matthes, E. Vardo, P. Schaaf
Chair Materials for Electrical Engineering and Electronics
Institute of Materials Science and Engineering
Institute of Micro and Nanotechnologies MacroNano
TU Ilmenau
Gustav-Kirchhoff-Str. 5, 98693 Ilmenau, Germany

K. Jaekel, H. Bartsch, J. Müller
Electronics Technology Group
Institute of Materials Science and Engineering
Institute of Micro and Nanotechnology MacroNano
TU Ilmenau
Gustav-Kirchhoff-Str. 1, 98693 Ilmenau, Germany

I. Gallino
Department of Materials Science and Engineering
Metallic Materials
TU Berlin
Ernst-Reuter-Platz 1, 10587 Berlin, Germany

 The ORCID identification number(s) for the author(s) of this article can be found under <https://doi.org/10.1002/adem.202302279>.

© 2024 The Authors. Advanced Engineering Materials published by Wiley-VCH GmbH. This is an open access article under the terms of the Creative Commons Attribution License, which permits use, distribution and reproduction in any medium, provided the original work is properly cited.

DOI: 10.1002/adem.202302279

technical limitations of the available conventional calorimeters. This restricted investigations to solid-state reactions within these materials. Only in the recent decade, reaction studies could be extended to higher heating rates with the help of nanocalorimetry—closer to the ones seen in SHS reactions where heating rates beyond 10^6 K s^{-1} are commonly observed.^[10] These investigations performed on Ni/Al nanometric multilayers were mostly performed with unreferenced and nondifferential nanocalorimeters.^[11–16] Thus, the heating rate is not constant during the experiment for cases where the released heat from the sample is higher than the heat that is lost to the surroundings. Since these factors depend on parameters such as the contact area to the surrounding, sample mass, and surrounding environment, the calorimetric results lack comparability as they are highly dependent on the used measurement setup. This complicates drawing direct connections between applied heating rates and the evolution of the reaction pathway observed via calorimetry. Hence, *in situ* experiments are often utilized, in which the films are deposited onto the sensor of the calorimeter. This makes them time- and cost-consuming, as each sample holder of a nanocalorimeter can only be used once. Further complications can arise from the use of shadow masks for sputtering on the sensor side of the nanocalorimeter, as it may change the microstructure at the edges of the sputtered regions.^[17] Due to these preparation steps for performing experiments, such approaches remained sparse with only a handful of experiments performed until this day.^[9,11–16,18]

In the present study, we focus on nanoscaled, free-standing Ni/Al multilayers produced by PVD via magnetron sputtering. For this purpose, we utilized the recently introduced fast differential scanning calorimeter (FDSC) Flash DSC 2+ from Mettler–Toledo (MT). However, unlike in previous research, where samples have been sputtered directly onto the sensor area of the nanocalorimeter chip, the samples are measured as nonadhered free-standing films without physical thermal contact. In contrast to previous experiments with custom-built nanocalorimeter setups, this method enables measurements of a multitude of samples taken from a single film using a single commercial nanocalorimeter sensor. Hence, we present FDSC experiment results for heating rates from 500 K s^{-1} up to $10\,000 \text{ K s}^{-1}$ utilizing the high-temperature UFH1 sensor. Furthermore, we were able to perform multiple measurements using one selected heating rate for statistical purposes. To correct for the thermal lag at the highest heating rates, a methodology is presented that compares the thermal lag of the nonadhered free-standing films with that of several adhered samples, such as several metallic glass formers and a low melting temperature Al-based alloy.

2. Results

2.1. Thermal Lag Estimation Methodology

2.1.1. Description of the Problem

Every calorimetric device relies on heat exchange between the sample material under investigation and the furnace. This complex 3-dimensional heat transfer problem is usually described by a single property called thermal lag to compare different

calorimetric devices and samples. In conventional calorimetry, samples are typically placed inside crucibles, which are then placed in the calorimeter furnaces. These consist of large silver blocks with embedded heating coils. In the case of the commercial MT FDSC 2+ nanocalorimeter, the function of the furnace is replaced by a microelectromechanical systems-based chip. Here, small heating electrodes embedded in a membrane control the temperature of the so-called active areas. Samples are typically placed in direct physical contact with the active area of the sensor. This is attained, e.g., by successively melting the materials above their liquidus temperature.^[19] This is not possible in cases where the first heating scan is important, e.g., the as-prepared state of the sample must be investigated during the first heating scan and its microstructure cannot be reproduced after melting in the FDSC and/or the maximum temperature of the device is below the melting temperature of the alloy under investigation.^[20] For polymer samples without direct thermal contact where the first heating scan is of importance for the analysis, a contact medium such as oil can also be used^[21] to establish a stable thermal contact. However, for free-standing multilayer films, the exothermic events finish at relatively high temperatures. Thus, oil cannot be used during the entirety of the heating scan because it thermally decomposes at higher temperatures. Consequently, the measurements in this work were performed without any form of contact medium. Due to the novelty of MT FDSC 2+, new methodologies still must be proven and established. So far there were no published studies involving measurements of free-standing multilayer films with FDSC without direct thermal contact. Studies using direct sputtering on the sensors have been limited to custom-built nanocalorimeters with selected investigations.^[10,14]

Due to the lack of direct thermal contact, the question arises if the thermal lag from the sensor to the sample during the measurements plays a crucial role. In the following, a methodology is presented that allows to calculate the thermal lag for the nonadhered, free-standing multilayer films, that are manually deposited on the active area of the sensor.

2.1.2. Methodology Description

Thermal gradients occur within a sample due to its finite thermal conductivity during temperature scanning experiments.^[22] These are present even with an ideal thermal contact between the sample and the sensor membrane. However, the thermal contact may not be ideal, e.g., for samples that cannot be intimately attached to the sensor membrane by repeated melting. Overall, these phenomena are commonly summarized under the term thermal lag, which causes an apparent shift of thermal events to higher temperatures in heating experiments^[23]—especially at higher heating rates. Conventionally, this offset is corrected by measuring the onset of melting of the alloy under investigation.^[24]

In general, the thermal lag, τ_{lag} , is characterized as a heating rate-independent time scale by the following equation^[25]

$$T_{\text{on}} = T_0 + q_{\text{H}} \tau_{\text{lag}} \quad (1)$$

T_{on} is the measured onset temperature of a heating rate-invariant thermal property, e.g., the melting temperature of an alloy, before any correction. As the slope of the linear equation, τ_{lag}

describes the time required for the heat transfer between the sample and the heater.^[26] T_0 is the extrapolated onset temperature for an infinitely small heating rate, $q_H = 0 \text{ K s}^{-1}$.

The multilayered films used in this study do not feature a heating rate-invariant thermal event that can be used to correct for τ_{lag} . Therefore, another method must be used to estimate the contact quality of the nonadhered multilayer films to the sensor membrane. Using the heat flow equilibration signal at the beginning of the first heating scan after the isothermal hold, the time or temperature interval required to reach a new steady-state temperature profile provides information about the thermal contact of the sample to the sensor substrate as well as the heat capacity, mass, and thermal conductivity of the sample.^[27] The heat flow equilibration signal at the beginning of the first heating scan in terms of the temperature interval, ΔT_{eq} , is analyzed by the tangent method, as shown in **Figure 1**. By using this value, it is possible to make a quantitative comparison to other systems where τ_{lag} can be determined through measurements of heating rate-invariant properties.

The results of the evaluation of ΔT_{eq} at the beginning of the first heating scan are shown in **Figure 2a** for different samples as indicated. The data points for the multilayered film samples were measured at least three times and averaged. In addition, for each sample, except the multilayer samples, τ_{lag} was determined based on the shift in the onset of the melting event using Equation 1. This shift is exemplarily shown for the case of the $\text{AlSi}_{10}\text{Mg}$ alloy in **Figure 2b**. With increasing heating rates up to $10\,000 \text{ K s}^{-1}$, the onset of the melting temperature shifts to higher temperatures. Using the linear fit from Equation 1, τ_{lag} is determined. In the case of the alloy shown, τ_{lag} has a value of 4.44 ms. Applying the same linear fit to the other samples yielded the values that are shown in **Figure 2a** behind the corresponding alloys. **Figure 2a** shows the expected trend that samples with higher thermal lag also show a stronger heating rate dependence of ΔT_{eq} . For multilayer film samples, the heating rate dependence of ΔT_{eq} is intermediate and lies in between samples that have shown a τ_{lag} value between 1.5 and 4 ms. To support the point that $\Delta T_{eq}(q_H)$ is useful for determining the average τ_{lag} of the multilayer film samples, it must be proven that both have a linear correlation with each other within the selected heating rate range. Thus, $\Delta T_{eq}(q_H)$ has been plotted as a function of the corresponding temperature shift of the melting temperature onset, $\Delta T_{m,on}$, for a given heating rate and sample in **Figure 2c**. The data points for $\Delta T_{m,on}$ have been taken from the linear fit rather

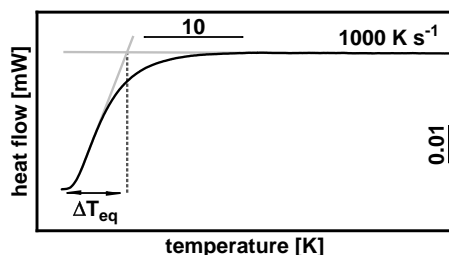


Figure 1. The start of a heat flow curve as a function of T shows the evaluation method of ΔT_{eq} during heating after isothermal hold.

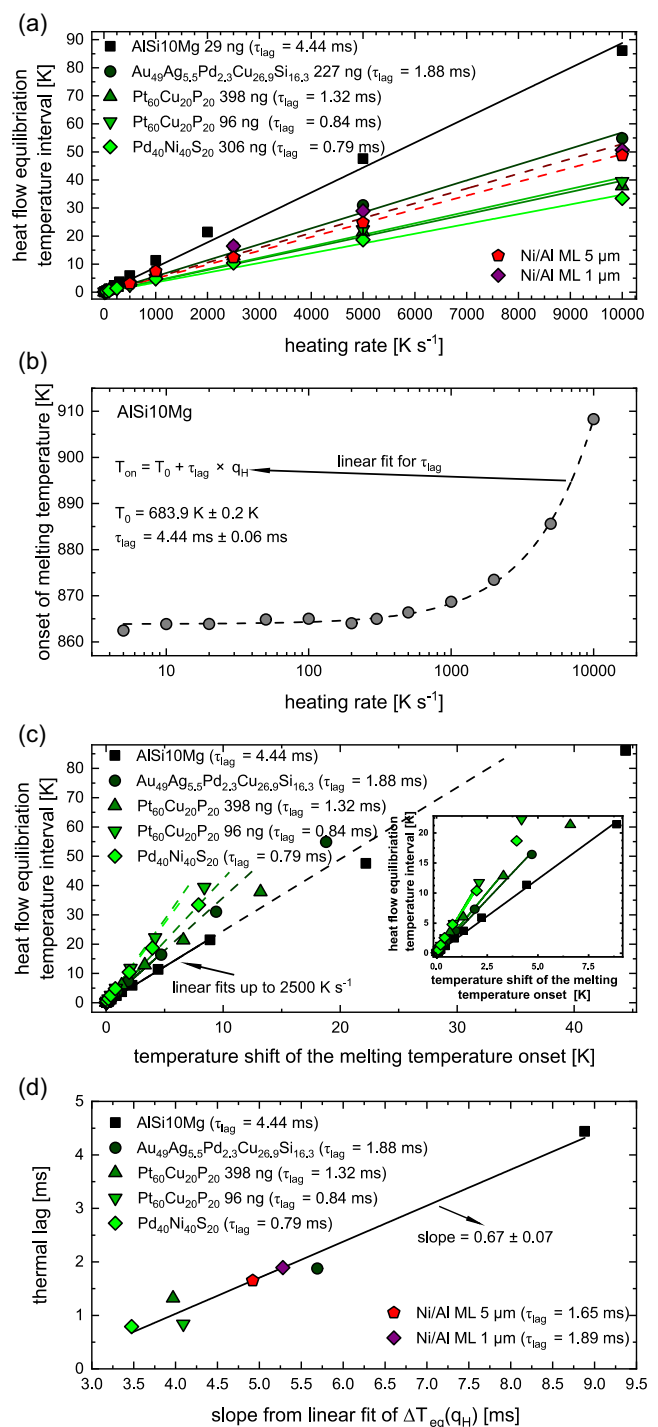


Figure 2. a) ΔT_{eq} as a function of q_H for different types of samples as indicated. b) The measured $T_{m,on}$ as a function of q_H exemplarily shown for the $\text{AlSi}_{10}\text{Mg}$ alloy. The linear fit shows the determination of the value for a sample. c) The results from (a) and (b) are combined for nonmultilayer samples to show the dependence of $\Delta T_{eq}(q_H)$ on $\Delta T_{m,on}$ for different samples. For all samples, data points for the same heating rate were correlated. d) The τ_{lag} results were correlated to the slope from the linear fits in (a) allowing the estimation of the average τ_{lag} for measurements with multilayer samples.

than the measured values to decrease the scatter in the data for lower heating rates. For each sample, the data have been fitted with a linear regression up to 2500 K s^{-1} . Each fit has a R^2 value above 0.99 confirming a high degree of confidence and thus the proportionality between both values up to this heating rate. At 5000 K s^{-1} and above a sublinear behavior is observed, i.e., the actual values for $\Delta T_{\text{eq}}(q_{\text{H}})$ are lower or the values for $\Delta T_{\text{m,on}}$ are higher than expected from the linear fit up to 2500 K s^{-1} . The reason for this deviation from the linear behavior is not yet entirely clear. However, it could be related to the tangent method used to determine the values for $\Delta T_{\text{eq}}(q_{\text{H}})$ and $T_{\text{m,on}}$.

Having shown the proportionality between $\Delta T_{\text{eq}}(q_{\text{H}})$ and $\Delta T_{\text{m,on}}$, up to a heating rate of 2500 K s^{-1} , the thermal lag of a certain sample is plotted in Figure 2d as a function of its slope of $\Delta T_{\text{eq}}(q_{\text{H}})$ derived from Figure 2a. The linear fit from all data points shows a positive correlation with a $R^2 > 0.97$. Based on the derived fit parameters, τ_{lag} can be determined for any sample even without any heating rate-independent thermal event. For the multilayers measured with the FDSC, the estimated τ_{lag} values are similar with 1.69 and 1.85 ms for the multilayers with a thickness of $t = 5 \mu\text{m}$ and $t = 1 \mu\text{m}$, respectively. It must be mentioned that the y -intercept of the fit function does not go through the origin, because even for a sample with zero thermal lag, the linear slope of $\Delta T_{\text{eq}}(q_{\text{H}})$ will be above 0, as the $\Delta T_{\text{eq}}(q_{\text{H}})$ for even an empty sensor also includes the thermal lag from the sensor itself that is not reflected in the measured thermal lag from the samples.

2.2. Calorimetric Results

The heat flow curves as a function of temperature for selected heating rates as indicated are displayed in Figure 3. A τ_{lag} correction was applied to the temperature axis of the heat flow curves for the FDSC measurements according to the τ_{lag} values derived in Section 2.1. To guarantee a better comparability across all

heating rates, the heat flow curves were normalized to the depth of the first exothermic peak. The two different colors red and purple indicate whether the FDSC measurement has been performed with the samples of $t = 5 \mu\text{m}$ or $t = 1 \mu\text{m}$, respectively. Only the FDSC scans performed with a constant heating rate above 2500 K s^{-1} (see violet dash-dotted curves) were obtained using multilayer films with $t = 1 \mu\text{m}$ instead of $5 \mu\text{m}$. Additional scans were performed using a conventional differential scanning calorimeter (DSC) with slow constant rates (below 1 K s^{-1}). These scans are added to Figure 3 as gray-colored heat flow curves for comparison.

As shown in Figure 3, the onset of interdiffusion and the following reaction peaks shift to higher temperatures with increasing heating rates. This behavior generally agrees with the character of thermally activated processes.^[28] This is the first time that more than five orders of magnitude of heating rates were covered by combining measurements acquired with different calorimeter devices. The standard deviation of the peak temperatures was below 10 K for almost all heating rates underlining the high measurement reproducibility.

At heating rates of 2500 K s^{-1} or higher, the reaction sequence appears to change from a three-stage to a single-stage mechanism (red curves). Films with $t = 1 \mu\text{m}$ show again the three-stage mechanism for the same heating rate.

However, a deviation from the constant heating rate of $10\,000 \text{ K s}^{-1}$ is seen in Figure 4 for the detected sample temperature suggesting that the enthalpy released from the sample led to an SHS reaction for $t = 5 \mu\text{m}$. Consequently, any measurements that showed a deviation of the sample heating rate from the programmed heating rate as exemplarily demonstrated in Figure 4 are discarded. However, to achieve these higher heating rates, samples with a smaller total thickness must be used, reducing the total mass, and thus, the total enthalpy released by the samples during the measurement. These measurements with samples of $t = 1 \mu\text{m}$ are shown as dash-dotted lines with purple

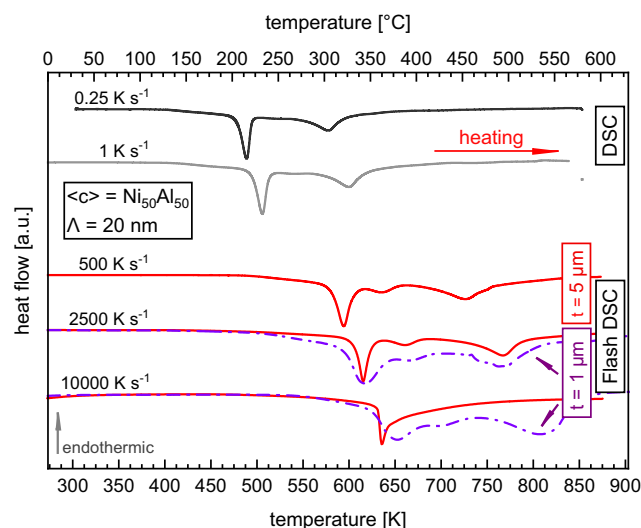


Figure 3. Heat flow curves measured with different heating rates as indicated. The gray and red curves correspond to DSC and FDSC measurements, respectively. The dash-dotted purple curves correspond to FDSC measurements of films with $t = 1 \mu\text{m}$ only.

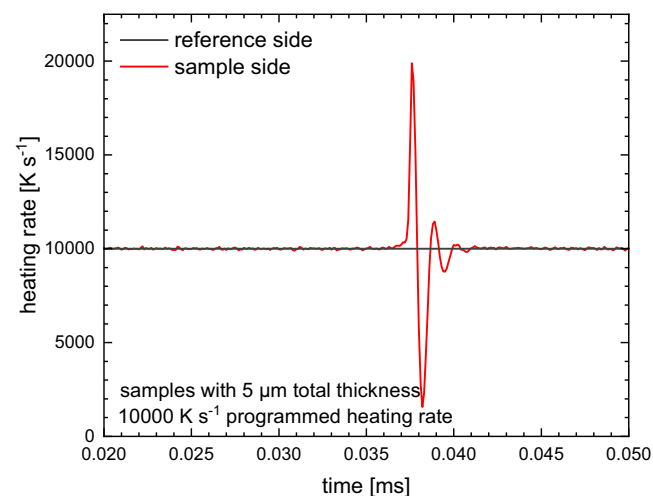


Figure 4. $q_{\text{H}}(t)$ shown for the reference and sample side in black and red color, respectively. The nanoscaled Ni/Al multilayer sample with $t = 5 \mu\text{m}$ was heated with a nominal $q_{\text{H}} = 10\,000 \text{ K s}^{-1}$. The heating rates are calculated from the detected temperatures on the reference and sample sides.

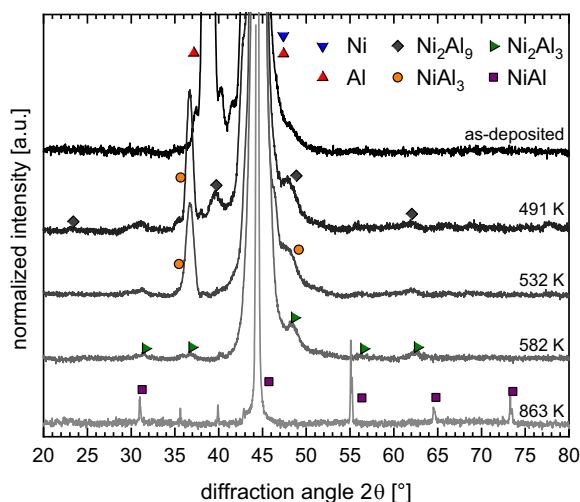


Figure 5. Normalized XRD intensity as a function of diffraction angle, 2θ . The different diffractograms were taken from samples heated up to the indicated temperature with 0.333 K s^{-1} . For reference, the as-deposited state is also shown. The symbols represent the phases as shown in the legend in the upper right corner.

color in Figure 3 and display the three-stage mechanism again. However, in contrast to measurements with samples of $t = 5 \mu\text{m}$, the heat flow curves are more smeared out.

2.3. X-ray Diffraction (XRD) Results

XRD studies of the multilayers after annealing in a conventional PerkinElmer DSC8500 with a slow heating rate of 0.333 K s^{-1} up to the designated temperatures and subsequent quenching to room temperature are summarized in Figure 5. The end temperatures for these heat treatments correspond to the three calorimetric peak temperatures seen in Figure 3 and the maximum temperature (863 K) during a DSC scan with 0.333 K s^{-1} . The X-Ray patterns suggest that only Ni and Al are present in the as-deposited conditions. After heating to 491 K, Ni_2Al_9 and Ni_2Al_3 have formed during the evolution of the first exothermic peak, in agreement with the literature. The Ni_2Al_9 reflexes that are present at 491 K disappear with further heating up to 532 K (2nd exothermic event). At a temperature of 582 K, which is at the third exothermic peak, the reflexes of Ni_2Al_3 appear at the expense of the NiAl_3 reflexes. After heating to the maximum temperature of 863 K, only the reflexes of the phase B2-NiAl are observed, and those of the pure elements have disappeared.

3. Discussion

3.1. Thermal Lag Correction Methodology

3.1.1. Comparison of Thermal Lag between Multilayer Films and the Other Samples

With the thermal lag determination study of free-standing films, it was shown that measurements with free-standing films have a thermal equilibration behavior similar to samples with a direct

thermal contact. The values for τ_{lag} for the different thicknesses of multilayer samples lie within the smallest and largest values of samples measured with a direct thermal contact. Hence, this method provides another pathway to correct the thermal lag-induced shift of thermal events for samples besides the deconvolution method used by Schawe and Schick for samples with a poor heat conductivity for DSC measurements.^[22]

Overall, this suggests that the thermal transport between the multilayer samples and sensor is fast enough for performing reliable calorimetric experiments. The values for the low-melting temperature alloys are in the same range as previous measurements for the thermal lag.^[24,26,29] The only exception is the value for the $\text{AlSi}_{10}\text{Mg}$ sample with 4.44 ms. However, this could be connected to the oxide layer formed on the surface of the particle during the powder manufacturing process reducing the thermal transport from sample to the sensor.

The high surface-to-volume ratio of the multilayered samples likely aids the fast thermal transport from the sensor into the sample and offsets the disadvantage of having no direct thermal contact for free-standing films. The multilayered samples have a surface-to-volume ratio, A/V , of $0.41\text{--}0.61 \mu\text{m}^{-1}$ for the sample with $t = 5 \mu\text{m}$ and $2\text{--}2.2 \mu\text{m}^{-1}$ for the samples with $t = 1 \mu\text{m}$. In contrast, the $\text{Au}_{49}\text{Ag}_{5.5}\text{Pd}_{2.3}\text{Cu}_{26.9}\text{Si}_{16.3}$ sample with a near-spherical shape has a $A/V = 0.16 \mu\text{m}^{-1}$ if a full sphere is assumed. It appears that the higher A/V ratio by a factor of 3 to 12.5 for the multilayer samples compensates for the lack of a direct contact compared to the other samples. In particular, the flat shape reduces the thermal gradient perpendicular to the sample bottom and yields an advantage compared to other shapes, since the Ar purge gas flow cools the samples from above during measurements. It needs to be pointed out that τ_{lag} of the free-standing multilayer film samples would still be higher in comparison to samples with direct thermal contact and a higher A/V ratio. In particular, for highly reactive Ni/Al multilayers, a further extension of the measurable heating rate range requires a further reduction of the sample mass by smaller total thicknesses. However, it is questionable whether such measurements via nonadhered, free-standing films would remain possible, since lighter samples become more susceptible to movements by disturbances (e.g., due to the applied Ar gas flow). Furthermore, the intrinsic stresses of the free-standing films vary with the total thickness of the samples^[27] and could complicate the measurements in regard to the thermal contact. To achieve trustworthy measurements at the highest possible heating rates of around $50\,000 \text{ K s}^{-1}$, it is likely required to rely on selected measurements of samples directly sputtered on the FDSC sensor with the thickness of only a few bilayers.

3.1.2. Influence of Thermal Lag Correction on the Apparent Activation Energy

Using the acquired calorimetric data from Section 2.2, a Kissinger analysis can be performed. This method was introduced in 1956^[30] and is generally used to perform a basic kinetic analysis for thermally activated processes. Using the peak temperatures, where the reaction rate for a single process is at its maximum, the apparent activation energy, E_A , of a single process can be determined via

$$E_A = -R \frac{\ln\left(\frac{q_H}{T_p^2}\right)}{\frac{1}{T_p}} \quad (2)$$

where R is the universal gas constant, q_H is the heating rate, and T_p is the peak or onset temperature of the analyzed event. Plotting $\ln(q_H/T_p^2)$ as a function of $1/T_p$, the activation energy can be determined from the slope of a linear fit.

In **Figure 6**, the Kissinger analysis before and after the thermal lag correction is shown. All analyzed processes appear to show monotonic Arrhenius behavior over the whole investigated range of applied heating rates without significant deviations.

Due to the small number of data points for each of the three individual calorimeter device and total sample thickness combination listed in **Table 1** and **2**, there is significant variation in the individual E_A values for a given exothermic event.

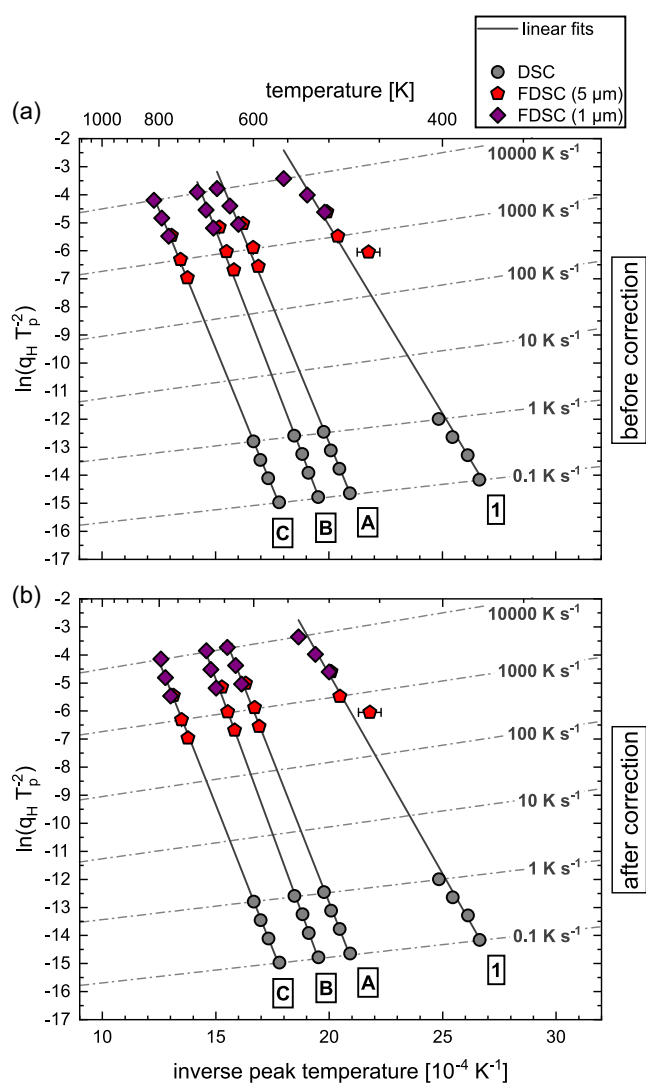


Figure 6. Kissinger plots for the interdiffusion (1) as well as the three exothermic events A, B, and C. a) The data before the τ_{lag} correction, and b) after applying the τ_{lag} correction. The linear fit in dark gray color represents the Arrhenius fits for each event covering all data points across the entire heating rate range.

Table 1. Overview of the determined apparent activation energies for the different thermal events before applying the temperature correction for τ_{lag} .

Selected data points for fitting	Apparent activation energy [eV]			
	Interdiffusion	Peak A	Peak B	Peak C
DSC	1.01 ± 0.09	1.63 ± 0.04	1.80 ± 0.06	1.66 ± 0.05
FDSC (5 μm)	0.61 ± 0.25	1.90 ± 0.23	2.06 ± 0.17	1.86 ± 0.01
FDSC (1 μm)	0.57 ± 0.06	1.14 ± 0.15	1.56 ± 0.09	1.72 ± 0.06
All data points	1.16 ± 0.06	1.69 ± 0.04	1.81 ± 0.03	1.71 ± 0.01

Table 2. Overview of the determined apparent activation energies for the different thermal events after applying the temperature correction for τ_{lag} .

Selected data points for fitting	Apparent activation energy [eV]			
	Interdiffusion	Peak A	Peak B	Peak C
DSC	1.01 ± 0.09	1.63 ± 0.04	1.80 ± 0.06	1.66 ± 0.05
FDSC (5 μm)	0.64 ± 0.29	2.19 ± 0.24	2.34 ± 0.28	2.04 ± 0.05
FDSC (1 μm)	0.79 ± 0.05	1.79 ± 0.18	2.70 ± 0.10	2.64 ± 0.10
All data points	1.23 ± 0.05	1.78 ± 0.02	1.90 ± 0.02	1.77 ± 0.02

The monotonic Arrhenius behavior in these types of plots was also previously observed during annealing for a HPT processed Ni–Al composite.^[9] Yet, other researchers suggest that a deviation from the Arrhenius behavior for FDSC measurements performed over large orders of magnitudes has to occur, independent of the material class.^[31] However, a non-Arrhenius behavior is often only observed for the rate-dependence of α -relaxation of (glass-forming) liquids.^[32] Here, Angell's fragility concept allows to classify supercooled liquids in terms of their degree of deviation from the Arrhenius behavior.^[33]

The importance of a thermal lag correction is highlighted by the fact that it significantly changes the determined E_A values for all thermally activated processes at the highest heating rates measured only with samples of $t = 1 \mu\text{m}$, as shown by the comparison of the E_A values listed in **Table 1** and **2**. Before a correction is applied, the change of the slope for the data points from the $t = 1 \mu\text{m}$ samples (purple diamonds) could indicate the onset of a change in the reaction mechanism. However, the data points from the $t = 1 \mu\text{m}$ samples as shown in **Figure 6b** appear to align better than before the thermal lag correction. This indicates that even for the highest heating rates, there is likely no change in the apparent activation energy for these thermally activated processes.

3.2. Comparison of Determined Apparent Activation Energies to Previous Literature

Upon annealing at elevated temperatures, the initially metastable system of pure Ni and Al layers will lower its Gibbs free energy of the system by interdiffusion followed by a series of phase transformations often involving the formation and growth of intermetallic phases. Ultimately, the final step in the evolution of these

micro- and nanoscale systems leads to the phase(s) expected by the equilibrium phase diagram for the overall composition of the system. To facilitate the formation of any intermetallic phase, it is well-known that the concentration gradient across the interfaces must be lowered. This is necessary to reduce the Gibbs free energy activation energy barrier that must be overcome to allow the local formation of a supercritical nucleus of the new phase.^[34] Usually, this is achieved by the formation of a (supersaturated) solid solution across interfaces—either across the phase boundaries or across the grain boundaries in each layer. Such a process is observed by calorimetry in the form of a shallow exothermic shoulder, usually related to the asymmetric interdiffusion of Ni and Al through the various fast diffusion pathways. The apparent activation energy for Al in Ni diffusion is almost twice that for Ni in Al.^[35] In the present Kissinger analysis, the value for the apparent activation energy is 1.23 ± 0.05 eV. Other studies have derived E_A values for solid-state interdiffusion between $0.59^{[11]}$ and 1.24 eV.^[36]

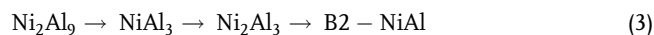
The value obtained here is in the upper range of previously measured apparent activation energies. However, since the values for bulk interdiffusion are still higher^[37] than the one derived in this work, it is plausible to assume that grain boundary diffusion is the dominant mechanism. The strong texturing observed for Ni/Al multilayers in this study, which is generally expected for face-centered cubic metals deposited by sputtering techniques,^[38] may also account for the high-than-expected apparent activation energy for interdiffusion observed here. The large variation in the reported E_A values likely has its origin in the different microstructures fabricated by the researchers: different bilayer thicknesses,^[36,39] different overall compositions,^[14,36] and different fabrication methods.^[11,40] Additionally, the different measurement techniques^[36,39–41] employed may also influence the measured E_A values. In addition, these studies were often limited to data from a small temperature and heating rate range, unlike our present study.

Michaelsen et al. also attributed the exothermic shoulder event to the growth of B2-NiAl.^[42] In comparison to our study, the E_A values (≈ 0.8 eV) are lower than the ones measured here. Neither the higher activation energies from our studies nor our XRD investigations suggest the formation of an intermetallic after deposition of the multilayer films. Furthermore, the B2-NiAl homogeneity stability region at low temperatures (≈ 673 K) is reported to be between 46 and 59 at%.^[43] The homogeneity region is expected to decrease even further at the low temperatures where the exothermic shoulder event is observed (≈ 373 – 474 K) in our study. However, kinetic constraints for the formation of the adjacent phases in the equilibrium phase diagram may extend the B2-NiAl stability region according to the T_0 concept. Moreover, the total molar enthalpy release of as-prepared samples measured here by DSC yields a value of -43.1 ± 0.5 kJ g-atom⁻¹. Assuming that the decrease in the total molar enthalpy release is entirely caused by B2-NiAl formation during deposition of the multilayers, this would suggest a mole fraction of ≈ 30 at%. This phase fraction should be also detectable by conventional XRD which is not the case here.

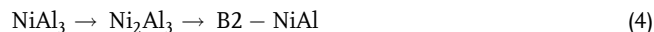
With further annealing, the formation of the first intermetallic phase is observed. In general, the calorimetric heat flow signature at low heating rates with three main exothermic events is similar to that observed by other groups also using sputtered

multilayers with identical bilayer periodicity and overall composition.^[44]

In the literature, the sequence of solid-state intermetallic phase formation sequence at low heating rates usually observed for Ni/Al multilayers is either



or



While the former has been observed for sputter-deposited multilayer films with $\Lambda > 20$ nm,^[45] the latter is often observed for multilayers prepared by evaporation techniques^[46,47] and in reactive Ni/Al systems prepared by either cold rolling,^[8] ball milling,^[40,48] or HPT processed films.^[9] In this work, the determined apparent activation energy for the first exothermic event is 1.78 ± 0.02 eV. Previous results typically suggest higher E_A values for the formation of the metastable, monoclinic η -Ni₂Al₉ phase^[49–51] compared to the formation of the NiAl₃ phase^[8,9,16,42,49]—when NiAl₃ is observed to form first. As the E_A value derived in this work is in between the values for both phases, it is assumed that both phases form simultaneously during the first exothermic event. The formation of the metastable phase besides NiAl₃ is further supported by the XRD results. However, as XRD has a detection limit for crystallite sizes, these results need to be confirmed by other techniques such as TEM.

Another important aspect is the fact that the reactions still take place entirely in the solid state, as evidenced by the absence of any endothermic melting event was observed with FDSC by Ivanisenko et al. for HPT-processed multilayers.^[9]

Increasing the heating rate from low values of $q_H = 0.1$ K s⁻¹ by five orders of magnitude does not change the phase transformation sequence in our FDSC experiments. The peak positions only shift to higher temperatures, as expected for thermally activated processes. This result is consistent with work published by other teams working on Ni/Al multilayers with small bilayer periodicities and equiatomic compositions using nondifferential nanocalorimetry in similar heating rate ranges.^[11–13] However, Swaminathan et al. observed a change in the number of exothermic events^[12] from 3 to 2 for heating rates above 10^4 K s⁻¹—just above the maximum possible heating rate in our studies. They interpreted this change as a transition from NiAl₃ as the first intermetallic phase to Ni₂Al₃ or a metastable bcc solid solution as the first phase.

However, these nondifferential nanocalorimetry experiments were mostly limited to a few selected heating rates and/or overall compositions and bilayer thicknesses. It must be emphasized that our approach using nonadhered multilayer films with the newly available commercial FDSC opens the possibility for easier access to nanocalorimetry data in the heating rate range up to at least 10^4 K s⁻¹. Second, the constant heating rate during these experiments allows reliable apparent activation energy data to be obtained using Kissinger analysis.

An extrapolation of all determined overall linear fits for the apparent activation energies suggests that no crossover is expected if this monotonic Arrhenius behavior remains valid over the next 1–2 orders of magnitude of heating rates. Assuming that there is no kinetic suppression of the formation

of the first phase, the two lines for interdiffusion and peak A would intersect at a heating rate of around and beyond 10^6 K s^{-1} . Coincidentally, this value is similar to rates that have been reported for the propagation of the reaction front of SHS in the Ni/Al system.^[52] However, there is a large uncertainty in such an extrapolation due to the small number of data points for the highest heating rates used here. It must be noted that the heating rate ranges under a controlled environment, i.e., constant scan rates, are not yet accessible with any commercially available nanocalorimeter device. Thus, the direct calorimetric observation of a polymorphic transition in binary multilayer films remains limited to decreasing the bilayer thickness below a certain threshold of the system ($<20 \text{ nm}$).^[53,54]

4. Conclusion and Outlook

We have shown that reproducible results via FDSC can be measured using the methodology presented here. Without the need for direct sputtering on the FDSC sensor, measurements up to 10^4 K s^{-1} were possible. Due to the nondirect thermal contact, data at the highest heating rates must be treated with caution and a temperature correction is necessary to obtain more reliable values. It is also important to check the sample and reference temperatures for the highest heating rates. Since the measurement is performed under constant heating rate conditions, the rapid heat release of the sample may lead to a violation of the null principle at some point during the measurement. However, potentially higher heating rates up to $5 \times 10^4 \text{ K s}^{-1}$ can be achieved with a less reactive system or sputtering directly onto the sensor area of the FDSC, which allows better heat transfer to the sensor. In general, this methodology allows easy application of the FDSC technique to a wide variety of material systems.

However, there are limits to the range of the heating rates that can be used with this FDSC device. The upper limit is set by the $q_{H,\text{max}} \approx 10^5 \text{ K s}^{-1}$ for empty sensors. For highly reactive samples, such as the equiatomic Ni/Al multilayer films used in this study, the highest achievable rates are determined by the rate, at which the sudden heat release causes a violation of the null principle. This can be circumvented either by using smaller total thicknesses, which reduces the mass and thus the absolute heat release of the samples, or by sputtering films directly onto the sensor area, which improves the thermal contact with the sensor. The lower limit is determined by the signal-to-noise ratio that still allows the detection of a useful heat flow signal. Theoretically, by using the low-temperature UFS1 sensor, the entire range of heating rates can be measured seamlessly, if the reactivity of the samples allows.

From the results of the FDSC measurements, we derived values for the apparent activation energy using the Kissinger analysis. Two

main points can be summarized: 1) This is the first time that E_A values of multilayer films have been analyzed over five orders of magnitude of heating rates using a single measurement technique, namely, calorimetry. This analysis can be extended to lower heating rates if desired. The differential setup also allowed experiments to be performed with a constant heating rate, which allows better conclusions to be drawn about the reaction mechanism, as there is a clearer relationship between heating rate and phase transformations compared to previous measurements with nondifferential calorimeter setups. This is useful for those who rely on the rapid acquisition of experimental apparent activation energy data for their theoretical modeling studies with multilayer films; and 2) Apparent activation energies in this study appear to follow a monotonous behavior from the slowest to the fastest heating rates.

A more comprehensive study, which is currently being carried out, includes more data points at intermediate heating rates using the low-temperature UFS1 chip by MT, bridging the gap to conventional calorimetry. In addition, there are still open questions: is the first phase formed at high heating rates the same as that formed at low heating rates? How does interdiffusion manifest itself microstructurally at higher heating rates in different stages? To address these questions, we will utilize the FDSC as a heat treatment tool, quenching the Ni/Al multilayer samples while precisely targeting specific temperature points in the phase transformation sequence to conduct ex situ experiments. Previous studies using nanocalorimeters often relied on in situ techniques to establish links to microstructural changes during heating or were relegated to ex situ observations after the entire reactions sequence had been completed. This technique will also be used in a series of ongoing calorimetric experiments on Ni/Al multilayer films with different bilayer thicknesses and overall compositions.

5. Experimental Section

Deposition Process of Ni/Al Multilayer Films: The deposition process for the fabrication of the Ni/Al multilayer films was performed by direct current (DC) magnetron sputtering on flat Si (100) wafers using a cluster deposition system CS400 by Von Ardenne. The deposition parameters are summarized in **Table 3**. Both targets by FHR Anlagenbau GmbH have a diameter of 100 mm and a nominal purity of 99.999 wt% for Al and 99.98 wt% for Ni. The individual layer thickness was achieved by a fixed deposition time per layer under consideration of the previously determined growth rate. This resulted in a bilayer periodicity, Λ , of 20 nm and an overall total composition of $\langle c \rangle = \text{Ni}_{50}\text{Al}_{50}$ (composition values always in at% unless otherwise stated). The free-standing films used for these experiments were obtained by carefully peeling the Ni/Al multilayers from the substrate.

Fabrication Process of Low Melting Metals: Several low-melting temperature alloys were used to determine the thermal lag: an $\text{AlSi}_{10}\text{Mg}$ powder ($\text{Al}_{90.16}\text{Si}_{9.36}\text{Mg}_{0.42}\text{Fe}_{0.06}$) from Concept Laser GmbH and the three

Table 3. Summarized deposition parameters used for the fabrication of the Ni/Al multilayer films with $\Lambda = 20 \text{ nm}$.

Target material	Substrate-to-target distance [mm]	Ar flow [mL min^{-1}]	Substrate temperature [K]	Power [W]	Working pressure [10^{-3} mbar]	Sputter rate [nm s^{-1}]	Individual layer thickness [nm]	Number of layers	Total thickness [μm]
Ni	105	30	298	200	5	0.33	8	250	5
Al						0.43	12		
Ni						0.33	8	50	1
Al						0.43	12		

metallic glass-formers $\text{Au}_{49}\text{Ag}_{5.5}\text{Pd}_{2.3}\text{Cu}_{26.9}\text{Si}_{16.3}$, $\text{Pt}_{60}\text{Cu}_{20}\text{P}_{20}$, and $\text{Pd}_{40}\text{Ni}_{40}\text{S}_{20}$. The later three were produced in the shape of ribbons with a custom-built melt-spinning device. The fabrication process for the metallic glass formers is described in more detail in refs. [55–57].

Calorimetric Investigations: For measurements with conventional calorimetry, several pieces of the multilayer films were stacked on top of each other to achieve the required signal-to-noise ratio. The mass for these measurements ranged from 1 to 4 mg. For measurements with the MT FDSC 2+, specimens were obtained by manually cutting a free-standing film to the desired size with a ceramic blade. Each specimen was manually placed on the sensor area of the sample side of a high-temperature (UFH1) chip sensor using a brush hair. The sample size was appropriately chosen to optimize the signal-to-noise ratio of the heat flow curves, i.e., larger samples for lower heating rates and smaller samples for higher heating rates. The estimated sample masses ranged from 10 to 100 ng based on the method described in ref. [9].

The MT DSC 3 was equipped with a Huber TC45 intracooler. The measurements were performed in a temperature range of 253 K up to 853 K in standard Al pans with different heating rates of 0.1, 0.25, 0.5, and 1 K s^{-1} . Each measurement consists of two up-scans with the same heating rate, where the second scan with the reacted material is used as baseline. The measurement cell was purged with a constant flow of 20 mL min^{-1} of high-purity Ar gas (99.9999 vol%). The device was calibrated for temperature and enthalpy of transformation for the applied heating rate and crucible using the melting signals of pure standard metals.

The heat treatments for the XRD experiments were performed with the PerkinElmer DSC8500 at a heating rate of 0.333 K s^{-1} to the specified maximum temperature and then quenched at 3 K s^{-1} . The instrument was calibrated and used in the same manner as for the MT DSC 3 measurements.

With the MT FDSC 2+, the heating rates of 500, 1000, 2500, 5000, and 10 000 K s^{-1} were probed. The samples were heated with a defined heating rate from 223 K to a maximum temperature of 873 K ($t = 5 \mu\text{m}$) and 1073 K ($t = 1 \mu\text{m}$) with the high-temperature UFH1 sensor. For each specimen, a baseline was obtained by performing a second up-scan with the reacted material. The MT FDSC 2+ was equipped with a Huber TC100 intracooler with the sensor substrate temperature set to 188 K. At each heating rate, the measurement was repeated at least three times to provide statistics. The FDSC cell was constantly purged with high-purity Ar gas (99.9999 vol%) at a rate of 20 mL min^{-1} prior to and throughout the measurement. The calibration of the chip sensor was ensured through the melting of pure elements as standards as explained in ref. [58] after all experiments had been performed.

The measurements necessary for the thermal lag correction and methodology were performed with a larger heating rate interval than for the multilayer films with the UFH1 sensor starting with 10 K s^{-1} up to 10 000 K s^{-1} . The measurements for the $\text{AlSi}_{10}\text{Mg}$ were performed with $q_{\text{H}} = 5, 1 \times 10, 2 \times 10, 5 \times 10, \text{ and } 10 \times 10^4 \text{ K s}^{-1}$ with $n = 1-3$. All the low-melting temperature alloy samples were repeatedly heated above their respective liquidus temperatures by about 100 K until a constant thermal contact with the sensor substrate had been established. The masses of those samples were determined from the melting events and derived based on the known literature values for the enthalpies of fusion.

XRD Experiments: The X-Ray diffractometer was a PANalytical X'Pert Pro using Cu-K α radiation ($\lambda = 0.15418 \text{ nm}$) in a diffraction angle range (2θ) between 20° and 80°. The voltage was 40 kV and the electron beam current was 40 mA. The instrument operated in Bragg–Brentano mode with a dwell time of 1 s per step and a step size of 0.02659°. The X'Pert HighScore Plus software was used to correct for the influence of CuK α radiation.

Acknowledgements

This study was supported by the Deutsche Forschungsgemeinschaft (GA 1721/3-1 and 3-2). K.J. and H.B. acknowledge financial support from the German Research Foundation (DFG) through grant BA 6161/1-1, and Y.H.S.C., S.M., and P.S. acknowledge financial support from the German Research Foundation (DFG – project numbers: 426206394 and 426362670) through grant Scha 632/29 (project number: 426206394)

and Scha 632/30 (project number: 426362670). Support by the Center of Micro- and Nanotechnologies (ZMN), a DFG-funded core facility (DFG grant Scha 632/27) of the TU Ilmenau, is gratefully acknowledged.

Open Access funding enabled and organized by Projekt DEAL.

Conflict of Interest

The authors declare no conflict of interest.

Data Availability Statement

The data that support the findings of this study are available from the corresponding author upon reasonable request.

Keywords

free-standing films, nanocalorimetry, Ni/Al multilayers, solid-state reactions, thermal lag

Received: December 30, 2023

Revised: April 12, 2024

Published online: May 11, 2024

- [1] C. Pauly, K. Woll, I. Gallino, M. Stüber, H. Leiste, R. Busch, F. Mücklich, *J. Appl. Phys.* **2018**, *124*, 195301.
- [2] I. Glassman, R. A. Yetter, N. Glumac, in *Combustion*, Academic Press, Waltham, MA **2015**.
- [3] J. Wang, E. Besnoin, A. Duckham, S. J. Spey, M. E. Reiss, O. M. Knio, M. Powers, M. Whitener, T. P. Weihs, *Appl. Phys. Lett.* **2003**, *83*, 3987.
- [4] J. C. Trenkle, T. P. Weihs, T. C. Hufnagel, *Scr. Mater.* **2008**, *58*, 315.
- [5] C. Rossi, K. Zhang, D. Esteve, P. Alphonse, P. Tailhades, C. Vahlas, *J. Microelectromech. Syst.* **2007**, *16*, 919.
- [6] S. Danzi, M. Menétrey, J. Wohlwend, R. Spolenak, *ACS Appl. Mater. Interfaces* **2019**, *11*, 42479.
- [7] A. G. Merzhanov, *J. Mater. Chem.* **2004**, *14*, 1779.
- [8] L. Battezzati, P. Pappaleopore, F. Durbiano, I. Gallino, *Acta Mater.* **1999**, *47*, 1901.
- [9] Y. Ivanisenko, A. Mazilkin, I. Gallino, S. S. Riegler, S. Doyle, A. Kilmametov, O. Fabrichnaya, M. Heilmaier, *J. Alloys Compd.* **2022**, *905*, 164201.
- [10] J. C. Trenkle, L. J. Koerner, M. W. Tate, N. Walker, S. M. Gruner, T. P. Weihs, T. C. Hufnagel, *J. Appl. Phys.* **2010**, *107*, 113511.
- [11] M. Vohra, M. Grapes, P. Swaminathan, T. P. Weihs, O. M. Knio, *J. Appl. Phys.* **2011**, *110*, 123521.
- [12] P. Swaminathan, M. D. Grapes, K. Woll, S. C. Barron, D. A. LaVan, T. P. Weihs, *J. Appl. Phys.* **2013**, *113*, 143509.
- [13] M. D. Grapes, T. LaGrange, K. Woll, B. W. Reed, G. H. Campbell, D. A. LaVan, T. P. Weihs, *APL Mater.* **2014**, *2*, 116102.
- [14] M. D. Grapes, M. K. Santala, G. H. Campbell, D. A. LaVan, T. P. Weihs, *Thermochim. Acta* **2017**, *658*, 72.
- [15] T. Neuhauser, G. Tinti, H. Leiste, N. Casati, M. Stüber, K. Woll, *Acta Mater.* **2020**, *195*, 579.
- [16] T. Neuhauser, G. Tinti, H. Leiste, N. Casati, S. Ulrich, M. Stüber, K. Woll, *Appl. Phys. Lett.* **2020**, *117*, 011902.
- [17] W. Decker, R. Belan, V. Heydemann, S. Armstrong, T. Fisher, in *Proc. of the Society of Vacuum Coaters 59th Annual Technical Conf.*, Indianapolis, IN, USA **2016**.

- [18] A. Wang, I. Gallino, S. S. Riegler, Y.-T. Lin, N. A. Isaac, Y. H. Sauni Camposano, S. Matthes, D. Flock, H. O. Jacobs, H.-W. Yen, P. Schaaf, *Mater. Des.* **2021**, 206, 109790.
- [19] M. Frey, N. Neuber, M. Müller, O. Gross, S. S. Riegler, I. Gallino, R. Busch, *Scr. Mater.* **2022**, 215, 114710.
- [20] M. Gao, J. H. Perepezko, *Thermochim. Acta* **2019**, 677, 91.
- [21] J. E. K. Schawe, *J. Therm. Anal. Calorim.* **2014**, 116, 1165.
- [22] J. Schawe, C. Schick, *Thermochim. Acta* **1991**, 187, 335.
- [23] G. Vanden Poel, V. B. F. Mathot, *Thermochim. Acta* **2006**, 446, 41.
- [24] S. Pogatscher, P. J. Uggowitzer, J. F. Löffler, *Appl. Phys. Lett.* **2014**, 104, 251908.
- [25] C. Schick, V. Mathot, in *Fast Scanning Calorimetry*, Springer International Publishing, Cham **2016**.
- [26] J. E. K. Schawe, *Thermochim. Acta* **2015**, 603, 128.
- [27] G. Abadias, E. Chason, J. Keckes, M. Sebastiani, G. B. Thompson, E. Barthel, G. L. Doll, C. E. Murray, C. H. Stoessel, L. Martinu, *J. Vac. Sci. Technol., A* **2018**, 36, 020801.
- [28] V. Pontikis, in *Diffusion in Materials* (Eds: A. L. Laskar, J. L. Bocquet, G. Brebec, C. Monty), Springer, Dordrecht, The Netherlands **1990**, p. 37.
- [29] J. E. K. Schawe, *Thermochim. Acta* **2021**, 698, 178879.
- [30] H. E. Kissinger, *J. Res. Natl. Bur. Stand.* **1956**, 57, 217.
- [31] S. Vyazovkin, *Molecules* **2020**, 25, 2813.
- [32] J. E. K. Schawe, *J. Chem. Phys.* **2014**, 141, 184905.
- [33] C. A. Angell, *Science* **1995**, 267, 1924.
- [34] B. Parditka, J. Tomán, C. Cserháti, Z. Jánosfalvi, A. Csik, I. Zizak, R. Feyerherm, G. Schmitz, Z. Erdélyi, *Acta Mater.* **2015**, 87, 111.
- [35] A. S. Edelstein, R. K. Everett, G. Y. Richardson, S. B. Qadri, E. I. Altman, J. C. Foley, J. H. Perepezko, *J. Appl. Phys.* **1994**, 76, 7850.
- [36] R. Grieseler, I. S. Au, T. Kups, P. Schaaf, *Phys. Status Solidi A* **2014**, 211, 2635.
- [37] Y. Du, Y. A. Chang, B. Huang, W. Gong, Z. Jin, H. Xu, Z. Yuan, Y. Liu, Y. He, F.-Y. Xie, *Mater. Sci. Eng. A* **2003**, 363, 140.
- [38] K. S. SreeHarsha, in *Principles of Physical Vapor Deposition of Thin Films*, Elsevier, Amsterdam, Boston **2006**.
- [39] G. M. Fritz, S. J. Spey, M. D. Grapes, T. P. Weihs, *J. Appl. Phys.* **2013**, 113, 014901.
- [40] J. M. Pauls, C. E. Shuck, A. Genç, S. Rouvimov, A. S. Mukasyan, *J. Solid State Chem.* **2019**, 276, 114.
- [41] J. P. Liu, J. Kirchhoff, L. Zhou, M. Zhao, M. D. Grapes, D. S. Dale, M. D. Tate, H. T. Philipp, S. M. Gruner, T. P. Weihs, T. C. Hufnagel, *J. Synchrotron Radiat.* **2017**, 24, 796.
- [42] C. Michaelsen, G. Lucadamo, K. Barmak, *J. Appl. Phys.* **1996**, 80, 6689.
- [43] H. Okamoto, *J. Phase Equilib. Diffus.* **2004**, 25, 394.
- [44] R. Knepper, M. R. Snyder, G. Fritz, K. Fisher, O. M. Knio, T. P. Weihs, *J. Appl. Phys.* **2009**, 105, 083504.
- [45] K. J. Blobaum, D. Van Heerden, A. J. Gavens, T. P. Weihs, *Acta Mater.* **2003**, 51, 3871.
- [46] E. Ma, C. V. Thompson, L. A. Clevenger, *J. Appl. Phys.* **1991**, 69, 2211.
- [47] X.-A. Zhao, H.-Y. Yang, E. Ma, M.-A. Nicolet, *J. Appl. Phys.* **1987**, 62, 1821.
- [48] M. R. Sharafutdinov, M. A. Korchagin, N. F. Shkodich, B. P. Tolochko, P. A. Tsygankov, I. Y. Yagubova, *Nucl. Instrum. Methods Phys. Res., Sect. A* **2007**, 575, 149.
- [49] K. Barmak, C. Michaelsen, G. Lucadamo, *J. Mater. Res.* **1997**, 12, 133.
- [50] A. S. Edelstein, R. K. Everett, G. R. Richardson, S. B. Qadri, J. C. Foley, J. H. Perepezko, *Mater. Sci. Eng. A* **1995**, 195, 13.
- [51] M. H. Da Silva Bassani, J. H. Perepezko, A. S. Edelstein, R. K. Everett, *Scr. Mater.* **1997**, 37, 227.
- [52] G. M. Fritz, J. A. Grzyb, O. M. Knio, M. D. Grapes, T. P. Weihs, *J. Appl. Phys.* **2015**, 118, 135101.
- [53] H. Aboulfadl, I. Gallino, R. Busch, F. Mücklich, *J. Appl. Phys.* **2016**, 120, 195306.
- [54] V. Ott, C. Schäfer, S. Suarez, K. Woll, F. Mücklich, H. J. Seifert, S. Ulrich, C. Pauly, M. Stueber, *Coatings* **2023**, 13, 149.
- [55] N. Neuber, O. Gross, M. Eisenbart, A. Heiss, U. E. Klotz, J. P. Best, M. N. Polyakov, J. Michler, R. Busch, I. Gallino, *Acta Mater.* **2019**, 165, 315.
- [56] O. Gross, S. S. Riegler, M. Stolpe, B. Bochtler, A. Kuball, S. Hechler, R. Busch, I. Gallino, *Acta Mater.* **2017**, 141, 109.
- [57] A. Kuball, B. Bochtler, O. Gross, V. Pacheco, M. Stolpe, S. Hechler, R. Busch, *Acta Mater.* **2018**, 158, 13.
- [58] X. Monnier, D. Cangialosi, B. Ruta, R. Busch, I. Gallino, *Sci. Adv.* **2020**, 6, eaay1454.